small methods

www.small-methods.com

Spray-Drying and Atomic Layer Deposition: Complementary Tools toward Fully Orthogonal Control of Bulk Composition and Surface Identity of Multifunctional Supraparticles

Stephan Müssig, Vanessa M. Koch, Carlos Collados Cuadrado, Julien Bachmann, Matthias Thommes, Maïssa K. S. Barr,* and Karl Mandel**

Spray-drying is a scalable process enabling one to assemble freely chosen nanoparticles into supraparticles. Atomic layer deposition (ALD) allows for controlled thin film deposition of a vast variety of materials including exotic ones that can hardly be synthesized by wet chemical methods. The properties of coated supraparticles are defined not only by the nanoparticle material chosen and the nanostructure adjusted during spray-drying but also by surface functionalities modified by ALD, if ALD is capable of modifying not only the outer surfaces but also surfaces buried inside the porous supraparticle. Simultaneously, surface accessibility in the porous supraparticles must be ensured to make use of all functionalized surfaces. In this work, iron oxide supraparticles are utilized as a model substrate as their magnetic properties enable the use of advanced magnetic characterization methods. Detailed information about the structural evolution upon individual ALD cycles of aluminium oxide, zinc oxide and titanium dioxide are thereby revealed and confirmed by gas sorption analyses. This demonstrates a powerful and versatile approach to freely designing the functionality of future materials by combination of spray-drying and ALD.

1. Introduction

Classically, the physical properties and functionality of nanoparticles are determined by their composition, size, and morphology. Multifunctionality in one spot can be obtained by combining different nanoparticles with distinct physical properties in one entity,[1–4] so-called supraparticles.[5,6]

It is very attractive to use solely wet-chemical methods to obtain nanoparticles as this comes with all flexibility to freely design composition, size, and morphology. However, wet-chemical approaches are not favorable in the same way for making complex entities, i.e., supraparticles. The reason is that wet-chemical assembly to supraparticles is strongly constrained by their chemical and physical interactions, which depend on the nanoparticles surface moieties, solvent environment, etc., and cannot be ignored or easily adjusted.[7–9]

Despite significant advances in the control of nanoparticle–nanoparticle interactions within supraparticles derived from wet chemical synthesis,[10–12] the processes do not provide the ultimate flexibility to combine arbitrarily chosen materials with each other.

To yield flexible and nearly unlimited combination options, forced assembly techniques provide a favorable strategy for nanoparticle assembly. Among these methods, we identified spray-drying, where nanoparticle dispersions are combined in a fine droplet and are ultimately forced to assemble when the liquid of the droplet is evaporated[13–15] as most promising. A wide variety of nanoparticle combinations within one supraparticle is thereby possible.[5,16,17] Thus, by means of spray-drying, physical

S. Müssig, K. Mandel
Department of Chemistry and Pharmacy
Friedrich-Alexander University ErlangenNürnberg (FAU)
Egerlandstraße 1, 91058 Erlangen, Germany
E-mail: karl.mandel@fau.de

V. M. Koch, J. Bachmann, M. K. S. Barr
Chair "Chemistry of Thin Film Materials" (CTFM)
Friedrich-Alexander University ErlangenNürnberg (FAU)
IZNF, Cauerstraße 3, 91058 Erlangen, Germany
E-mail: maissa.barr@fau.de

The ORCID identification number(s) for the author(s) of this article can be found under https://doi.org/10.1002/smtd.202101296.

DOI: 10.1002/smtd.202101296

C. Collados Cuadrado, M. Thommes
Department of Chemical and Bioengineering
Institute of Separation Science and Technology
Friedrich-Alexander-University Erlangen-Nürnberg
Egerlandstr. 3, 91058 Erlangen, Germany
E-mail: matthias.thommes@fau.de

J. Bachmann
Institute of Chemistry
Saint Petersburg State University
Universitetskii pr. 26, Saint Petersburg 198504, Russian Federation

K. Mandel
Fraunhofer Institute for Silicate Research ISC
Neunerplatz 2, 97082 Würzburg, Germany

attributes, carried by different nanoparticle types, are brought together in very unconventional combinations.[18] The supraparticles produced typically exhibit sizes of 1–20 μm[5] with a size distribution that is affected by the size of the used nanoparticles and process parameters such as spray-drying temperature. This relatively broad size distribution might be seen as a disadvantage for some applications; however, the polydispersity is often of subordinate importance as the functionality typically arises from within individual supraparticles by coupling, emergence, or colocalization.[5]

Moreover, the structural arrangement of the nanoparticles within the supraparticles can be controlled to a certain extent either by the process parameters[19] or by using templating approaches.[20,21] Additional information on different supraparticle morphologies is found in our review article.[5]

Taken together, forced assembly of distinct nanoparticles by means of spray-drying in a well-controlled process parameter set yields unique combinations of physical properties and structural arrangements of nanoparticles in one supraparticulate entity.

However, the outer (microparticles surface) and in particular inner surface (nanoparticles surface within the microparticles), and thereby the interfacial nature of these nanostructured and typically porous supraparticles, cannot be well defined yet. That is because the surfaces of the nanoparticles originate from their respective synthesis history.

This work demonstrates how to modify all surface functionalities in supraparticles independently of the synthesis history. The key toward achieving this goal is to combine the flexibility of spray-drying (which allows for adjusting the physical "bulk" properties of a supraparticle entity and its structure) with the flexibility and precision of atomic layer deposition (ALD). ALD as a chemical coating method controlled by individual surface reaction steps repeated in a cyclic manner enables one to coat not only planar substrates but also highly porous ones in a conformal manner. When applied to supraparticles, it can fully camouflage the interface on AND within the porous nanostructure with a surface/interface of almost any desired material.

In the following piece of work, the structural and chemical evolution of the supraparticle assembly upon repeated ALD cycles is monitored in a highly sensitive manner by magnetic and gas sorption measurements. We demonstrate that spray-drying and ALD represent tools the combination of which achieves a fully orthogonal control of bulk composition and surface identity in multifunctional supraparticles. Achieving this means that the physical properties (defined by the nanoparticles), the structural arrangement (of the supraparticles in dependence of the nanoparticle combination), and the surface nature of the nanostructure/supraparticles external and internal surfaces can be engineered fully independently, potentially offering very exotic material effects in one single entity (**Figure 1**).[22]

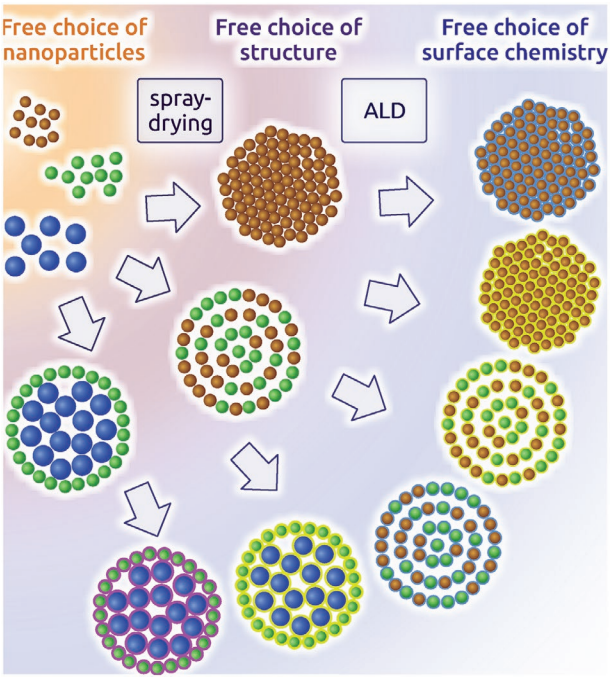

Figure 1. Versatility of the approach presented in this work. First, full control of physical properties is achieved by the choice of the nanoparticles used. Second, they can be arranged into supraparticles of various geometric structures by spray-drying. Third, their surface is chemically adjusted by atomic layer deposition (ALD), ultimately yielding highly flexible material compositions with multifunctional properties in one entity.

2. Results and Discussion

2.1. Functionalization of Supraparticles by ALD

To synthesize exotic material combinations, understanding the deposition via ALD on supraparticles is crucial. As a model particle system, supraparticles consisting of superparamagnetic iron oxide nanoparticles are synthesized. Subsequently, varying numbers of aluminum oxide (Al_2O_3) ALD cycles are deposited as a model deposition material. The surface chemical control of ALD allows one to increase the thickness of the coating with atomic precision cycle after cycle, as schematically illustrated in **Figure 2**.

ALD is based on the repetition of well-defined surface reactions between two (or more) molecular precursors and the surface that are self-limiting and complementary. A typical ALD process consists of four distinct steps: 1) The first precursor A reacts in a self-limiting manner with the reactive functional groups (e.g., −OH groups) on the substrate surface. 2) Excess of precursor A and gaseous by-products are purged out of the deposition chamber. 3) The second precursor B reacts in a self-terminating way with the adsorbed species of precursor A on the surface. 4) The excess of precursor B and gaseous by-products are purged away. These four steps conclude one ALD cycle[23–25] (Figure 2). Due to the self-limiting nature of the process, ALD yields highly conformal coatings on planar and high-aspect ratio substrates with atomic-scale thickness control.[26–28] As the iron oxide nanoparticles used here with diameters of ≈10 nm form the porous supraparticles, which in turn possess a diameter of a few micrometers, a geometrically restrictive porous network must be present. To allow the gaseous reactants to penetrate narrow structures, sufficiently long pulse and exposure durations during ALD are crucial.[29] Importantly, the surface modification of all nanoparticle surfaces, internal and external, is essential for optimized material properties with respect to their applications. Thus, it is crucial but challenging to understand whether ALD occurs on the internal surface

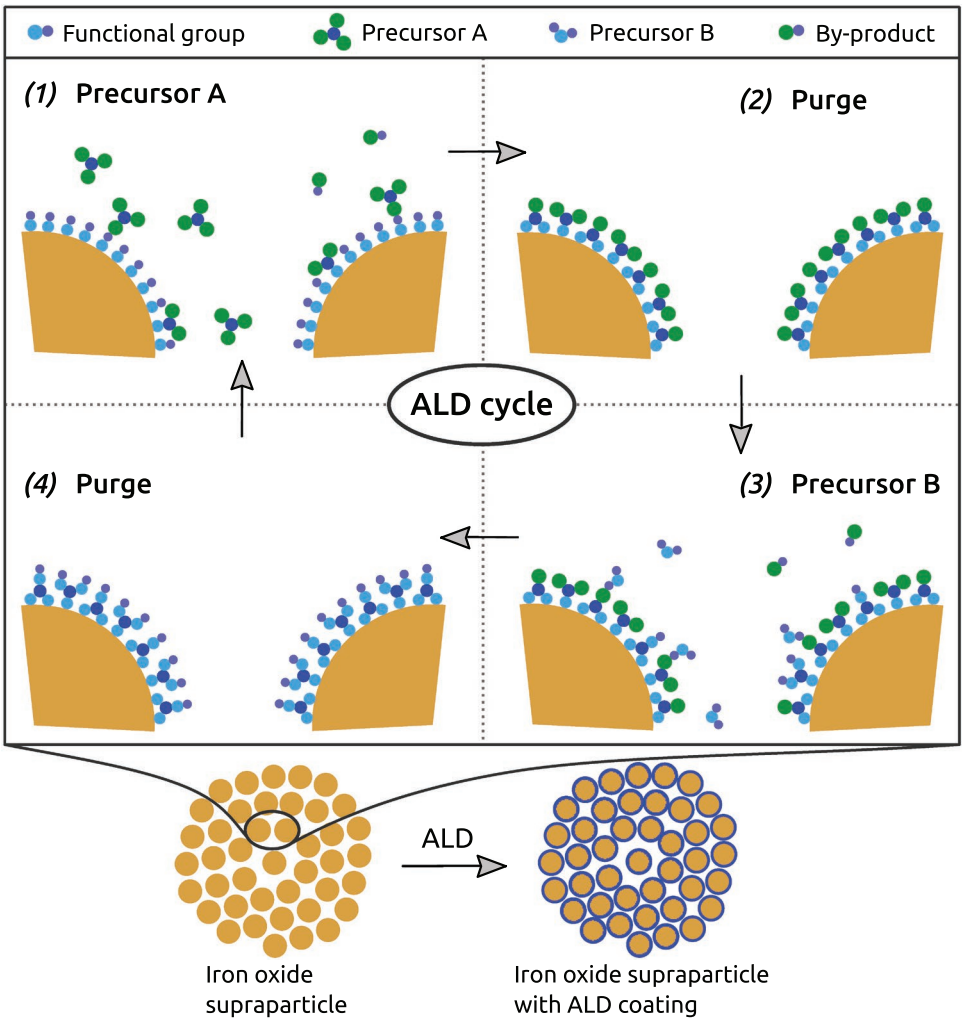

Figure 2. Scheme of ALD on supraparticles. The zoom illustrates the self-limiting growth of the coating in atomically thin layers of the coating material on the surface and interstices of supraparticles during one ALD cycle.

(i.e., all nanoparticle surfaces) of the supraparticles or on their external surface (i.e., surface of the microparticle) only.

A scanning electron microscopy image (**Figure 3**a) shows the external surface of the micrometer-sized supraparticles after ten cycles of Al_2O_3 deposition. Because the maximum Al_2O_3 layer thickness potentially deposited on the supraparticle structure after ten cycles is only about 2.1 nm (determined by spectroscopic ellipsometry on a silicon wafer placed inside the powder bed during ALD, which is assumed to be covered with 100% of available material), successful deposition, especially on the internal surface of the supraparticles, can hardly be confirmed by imaging methods. It should be noted that the experimentally measured Al_2O_3 film thickness of 2.1 nm deviates from the commonly accepted value of 1.1–1.2 nm (considering the theoretical growth rate per cycle (GPC) of 1.1–1.2 Å/c for Al_2O_3 ALD[30] determined in ideal conditions on exclusively planar substrates. Our experimentally determined value is likely affected by imperfect purging in the high specific-area system (nanopowder) considered here.

To analyze whether deposition is also feasible in the inner part of the porous supraparticles, a cross-section of such supraparticles (Figure 3b) is analyzed. The energy-dispersive X-ray (EDX) profiles (c) obtained by a line scan (d) identify oxygen, iron, carbon and, most importantly, also aluminium in the volume analyzed. Notably, aluminium is detected in the center of the supraparticle with similar intensity compared to the periphery, suggesting a homogeneous deposition on the external surface but most importantly also on the internal surfaces within the porous network.

2.2. Magnetic Measurements as a Tool to Deduce Information About the Structural Evolution

If the deposition is successful, the mass added in the thin film will influence the magnetic properties of the nanoparticles in the supraparticles in a quantifiable manner. In conventional wet-chemical functionalization approaches, the chemical surface of nanoparticles would be modified as well. However, this would be done before their assembly and not afterwards as it is done here. To investigate the influence of a modified chemical surface on the magnetic properties of such assemblies, their surface modification *after* assembly is essential. Upon surface modification before assembly, its effect on the

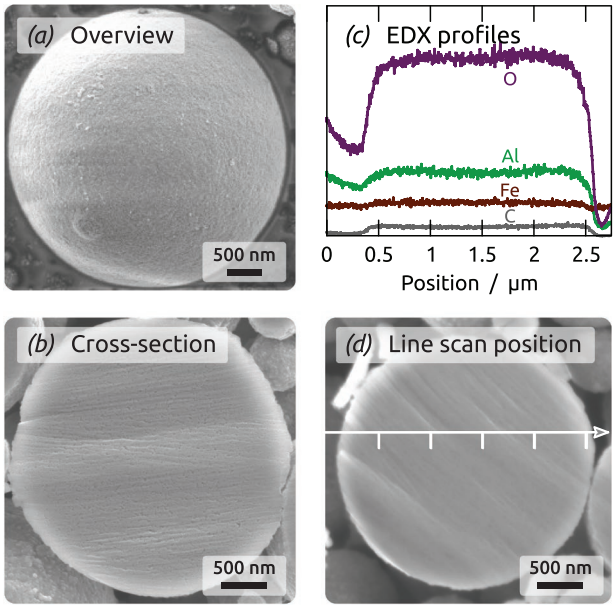

Figure 3. a) Scanning electron overview microscopy image and b) cross section of an iron oxide supraparticle after ten cycles aluminum oxide deposition with ALD. c,d) The EDX spectrum obtained shows aluminium along the whole line scan in the supraparticle, suggesting homogeneous deposition of aluminum oxide on the outer surface and importantly also on the inner surface within the supraparticle.

magnetic properties is mostly accompanied by a change in the particle–particle distance of magnetic nanoparticles during their assembly.[31,32] These two influential parameters can barely be adjusted individually by wet chemical methods, because the variation of different surfactants, stabilizers, or salts during synthesis and/or assembly changes both the spacing between nanoparticles and chemical identity at the surface of nanoparticles. Using ALD *after* assembly decouples structural from physical or chemical effects on nanoparticle–nanoparticle interactions. Therefore, the influence of chemical surface changes can be studied in detail and consequently, the ability of ALD to modify the interface identity of supraparticles is demonstrated.

For quantitative analysis, magnetization curves of superparamagnetic iron oxide supraparticles with varying numbers N of ALD cycles are analyzed (**Figure 4**a). The maximum magnetization (saturation magnetization, M_s) of the samples decreases with an increasing amount of diamagnetic material deposited. The decrease in M_s observed thus confirms the aluminum oxide deposition observed by EDX (Figure 3c). Plotting M_s as a function of of ALD cycle numbers performed (Figure 4b) consequently allows us to analyze the masses of deposited material. The saturation magnetization M_s decreases rapidly by 12 wt% from 67 to 59 emu g^{-1} upon deposition of the initial ten cycles (nominally 2.1 nm) of aluminum oxide. This suggests deposition of 12 wt% aluminum oxide mass with respect to the iron oxide mass. Afterward, M_S reaches a plateau until 150 cycles (the maximum cycle number considered in this study).

A similar trend is observed for zero-field-cooled/field-cooled (ZFC/FC) measurements of samples with different ALD cycles. In such measurements, samples are cooled to low temperatures (30 K) with no magnetic field present. Subsequently, the magnetic moment is monitored as a function of temperature upon heating under a small magnetic field (1 mT). During heating, a maximum is observed for superparamagnetic particles. The maximum occurs at the so-called blocking temperature T_B, which indicates the temperature above which the particles behave superparamagnetically. T_B generally depends on the nanoparticles used, their interactions, as well as their surface properties.[17,33] In the system studied here, a shift of T_B from 210 K toward higher temperatures is observed with progressing ALD cycles (Figure 4c). As the particle–particle distances of iron oxide nanoparticles within the supraparticles are unchanged during ALD, the shift of T_B can be interpreted as a tool to analyze the change in surface properties of the iron oxide nanoparticles, and thereby indirectly analyze ALD. This is due to a change in the magnetic properties of the supraparticles rather than due to the direct magnetic properties of Al_2O_3, as Al_2O_3 exhibits completely different behavior in such measurements (see ZFC/FC measurements of Al_2O_3 on diamagnetic silica supraparticles in Figure S1, Supporting Information).

From both magnetic measurement types, several conclusions can be drawn. First, deposition of aluminum oxide is confirmed quantitatively from the very first cycle. As it is very challenging to assess the deposition of very few cycle numbers via ALD experimentally, this demonstrates the potential of magnetic measurements as an additional and practical characterization method. Second, both the decrease in M_S and the shift in T_B occur rapidly during the initial ten ALD cycles before they reach a plateau phase. This indicates a rather abrupt change in the characteristics of deposition between the initial ten cycles and the subsequent ones.

The logical interpretation of this sudden and almost complete stop in deposited mass is pore clogging within the supraparticles as a result of coating and concomitant reduction of the interstice openings within each supraparticle. Once the internal surface is not accessible any more by the gas precursor molecules during ALD, no further deposition can occur on such surfaces. When the pores are clogged and deposition occurs only on the external surface of a 2.5 µm sized supraparticle, the mass of a nanometer thick atomic layer represents much less than 1% of the total particle mass. Thus, the deposition of such low masses appears as a seeming stop of deposition, similar to the trend observed from the data in Figure 4.

2.3. Gas Sorption Analyses of the Pore Evolution

To investigate this structural evolution in more detail, gas sorption measurements were performed. N_2 isotherms at 77 K for the pristine iron oxide supraparticles and impregnated with aluminum oxide by ALD at different cycles are shown in **Figure 5**a. The N_2 adsorption measurements exhibit type IV adsorption isotherm exhibiting pore condensation with a type H2 hysteresis loop.[34] This form of hysteresis can be attributed to adsorption metastability (affecting the adsorption branch) and pore network effects on desorption, indicative of pore constrictions and ink-bottle type pores, which lead to pore blocking during evaporation of the condensed liquid-like fluid from the pore cavities.[35,36] Hence, for type H2 hysteresis the desorption branch contains information about the pore neck-size distribution, while the pore/cavity size distribution can be obtained from the adsorption

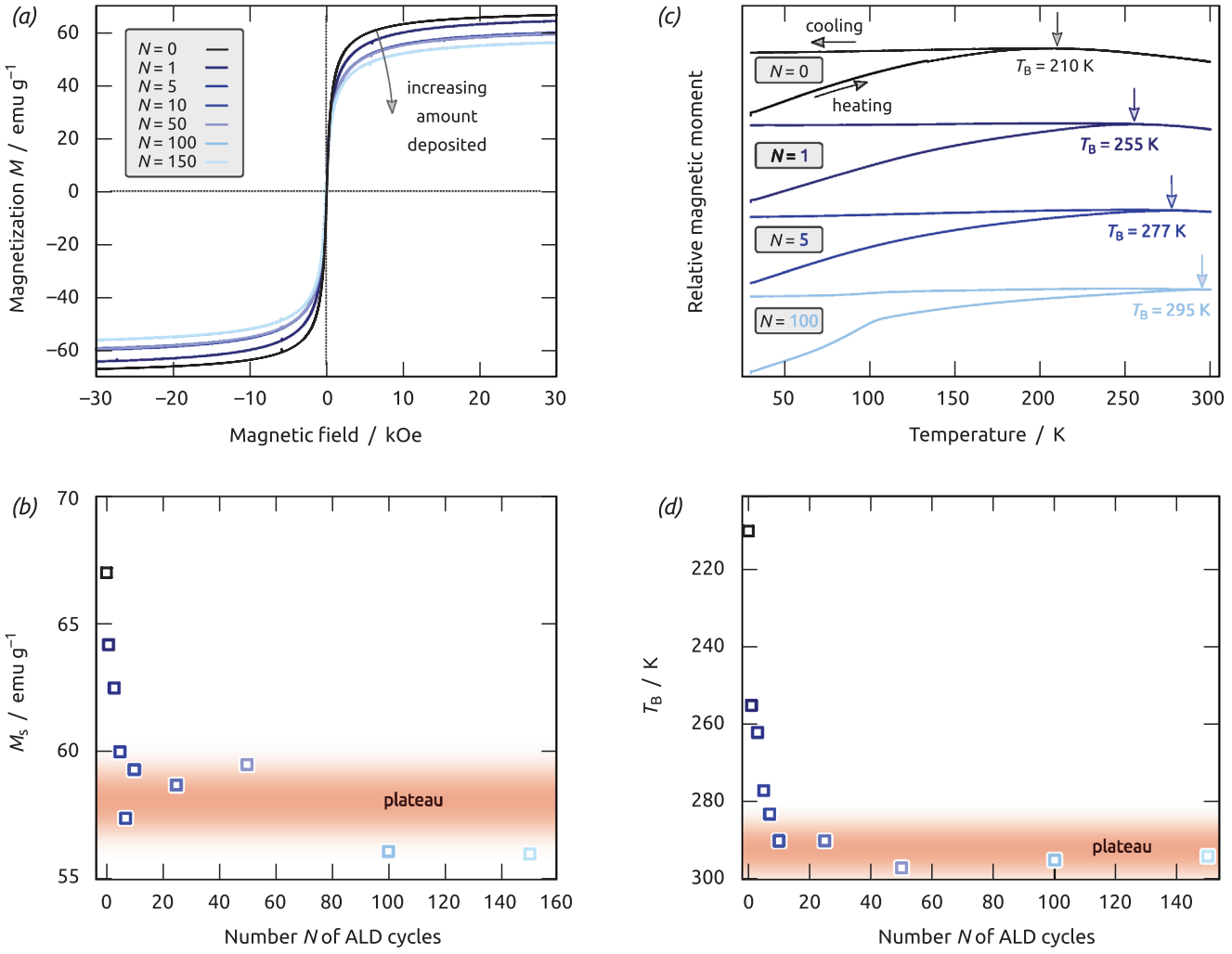

Figure 4. a) Magnetization curves of iron oxide supraparticles reveal a qualitative decrease in magnetization with increasing number N of ALD cycles. b) Upon plotting the saturation magnetization M_s as function of N, an initial rapid decrease of M_s is observed before it reaches a plateau phase after ≈10 cycles. c) Temperature-dependent zero-field-cooled/field-cooled (ZFC/FC) measurements reveal an increase in blocking temperature T_B with progressing ALD. d) Quantifying this shift as a function of N reveals a similar trend as for M_s, indicating different structural changes before and after ≈10 cycles.

branch (will be described in more detail below in context with Figure 5). A characteristic feature of a type IV isotherm is also the existence of a plateau, indicating that the mesopores are completely filled with condensed nitrogen. As can be clearly seen from the adsorption isotherms, this plateau, i.e., the maximum N_2 uptake, decreases significantly with increasing aluminum oxide deposition (i.e., increasing number of ALD cycles).

Figure 5b shows the pore size analysis for selected materials, i.e., for pristine iron oxide supraparticles and samples obtained after one and five cycles ALD. The pore size/volume distributions are calculated from the adsorption data by applying a dedicated nonlocal density functional theory (NLDFT) method, assuming cylindrical silica pores kernel to the adsorption branch. The adsorption branch kernel applied takes into account correctly that pore condensation occurs delayed due to metastable pore fluid.[37–39]

Pristine iron oxide particles show a broad pore size distribution (PSD), covering a range between 2.5 and 12 nm with the most frequent size (mode pore diameter) centered at 6.7 nm. Interestingly, deposition of aluminum oxide during the first ALD cycles seems not to affect the position of the pore size distribution curve significantly, which remains at 6.7 nm. On the other hand, as expected, the specific cumulative pore volume decreases with increasing aluminum oxide deposition.

From the nitrogen data, Brunauer–Emmett–Teller (BET) surface area and pore volume are calculated for the evaluated samples (Figure 5c). The deposition of aluminum oxide yields a decrease in both specific surface area and (specific) pore volume due to the filling of the porosity. Nevertheless, after the initial ALD cycles (1 and 5), open porosity remains, meaning that there are still empty pore channels which allow gas diffusion towards the inner and larger mesopores. On the other hand, for the samples with more ALD cycles, the decrease of the BET surface area and mesoporous volume is significantly accentuated. Particularly for the ten ALD cycles sample, only

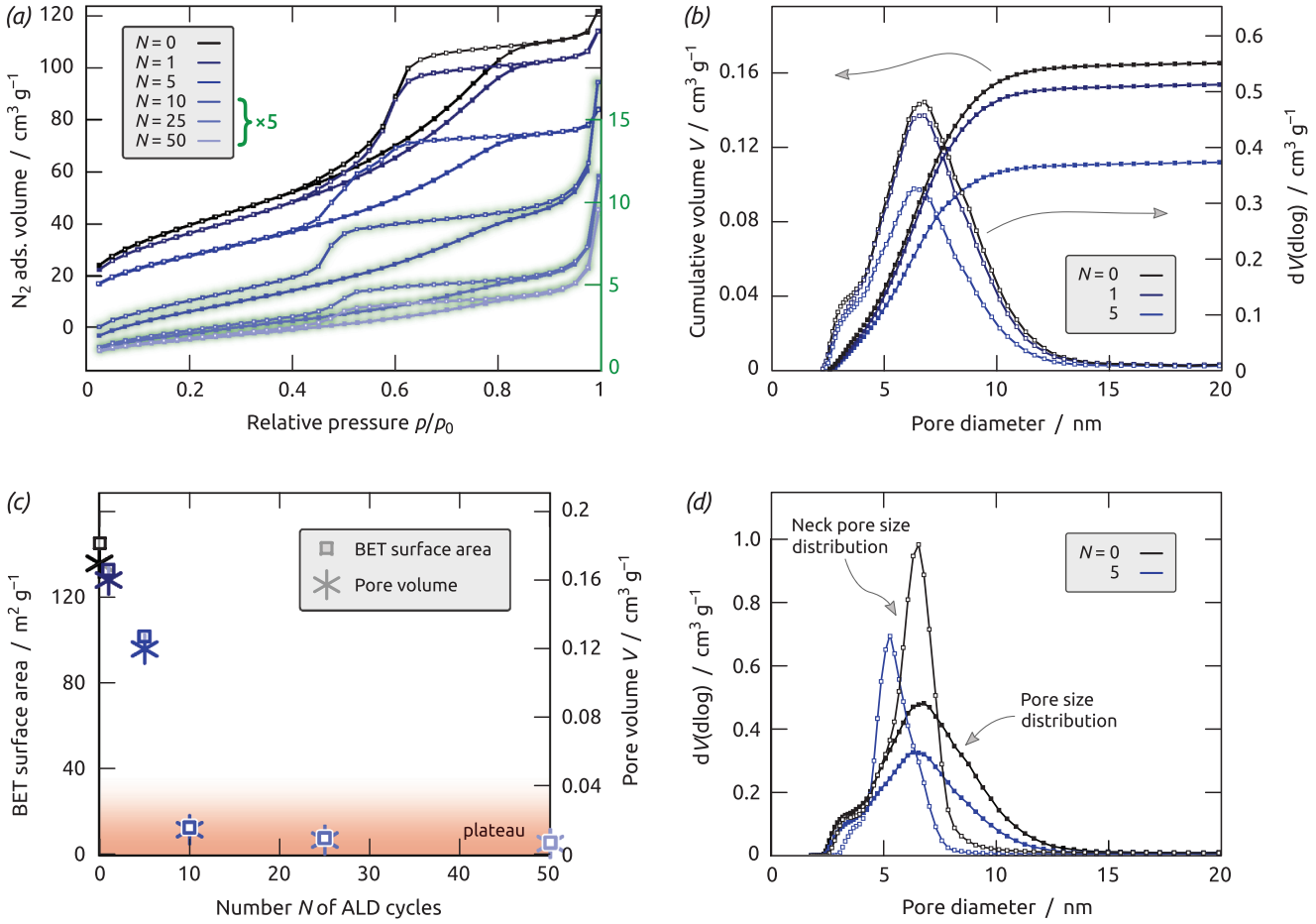

Figure 5. a) N_2 adsorption (full symbols) / desorption (open symbols) isotherms at 77 K for the iron oxide supraparticles after different numbers *N* of ALD cycles. b) NLDFT pore size analysis (differential PSD and cumulative pore volumes) for selected samples. c) Textural properties of iron oxide supraparticles after different values of *N*. d) NLDFT pore size distribution for the pristine iron oxide supraparticles and after five ALD cycles calculated from the adsorption (full symbols) and desorption (empty symbols) branch of the N_2 isotherms.

a minor amount of the original pore volume/surface area is accessible with a surface area reduction of 91% compared to the pristine sample.

Interestingly, and in complete congruence with the magnetic measurements, after ten ALD cycles, pore volume and surface area no longer change significantly, again indicating that after ten ALD cycles, the pores are mostly filled. For the 25 and 50 cycles, the aluminum oxide seems to be deposited on the external surface only. The external coating of the supraparticle becomes thicker without changing the internal porosity.

Important information concerning the effective change of accessible pore structure upon depositing aluminum oxide in individual ALD cycles can also be obtained by a more detailed analysis of the hysteresis loops determined. As mentioned, a type H2 hysteresis is observed, which is indicative of the presence of pore constrictions and/or ink-bottle pores. In such a case, the desorption branch of the hysteresis loops is affected by the pore blocking/percolation effect. Hence, the pore size (cavity) distribution is obtained, as already described from the adsorption branch by the application of a dedicated NLDFT kernel (Figure 5b). On the other hand, information concerning the neck size distribution can be obtained from an analysis of the desorption branch.

Figure 5d shows a comparison of the NLDFT pores size distributions obtained from adsorption and desorption for pristine iron oxide supraparticles and after five ALD cycles. It can be clearly seen that the PSD from desorption (empty symbols) is much narrower than from the adsorption branch (full symbols). This indicates that large pore widths between 7 and 12 nm are connected to the external surface through narrower pores, causing a delay in the N_2 evaporation process in cavities larger than 7 nm (pore blocking/percolation). We note the stark contrast between this case and unrestricted cylindrical pores, where the NLDFT pore size distribution obtained from adsorption and desorption branches would match.[35,36,39,40] As shown in Figure 5d, the PSD from the adsorption branch gives information concerning the intrinsic pore size distribution, while the PSD calculated from the desorption branch reveals particularly the distribution size of the pore necks/constrictions.

Interestingly, the incorporation of aluminum oxide by five ALD cycles into the iron oxide supraparticles seems only to have a small effect on the position of the intrinsic pore size distribution curve, while there is a significant shift in the mode pore diameter obtained from the desorption branch, reflecting a decrease in the effective neck diameters. For the five ALD

cycles sample, the peak shifts from 6.5 to 5.2 nm, meaning that the neck size shrinks by about 1.3 nm. With subsequent ALD cycles, the effective neck sizes decrease further as indicated by the observation of cavitation-induced evaporation leading to a type H4 hysteresis (according to IUPAC)[34] for the adsorption isotherm obtained after ten ALD cycles (Figure 5). In fact, if the neck diameter is smaller than a critical size (estimated to be ≈5–6 nm for nitrogen at 77 K), the mechanism of desorption from the larger pores involves cavitation (i.e., the spontaneous nucleation and growth of gas bubbles in the metastable condensed fluid).[38]

2.4. Model of the Structural Evolution during ALD

The complementary and consistent data obtained by SEM-EDX, magnetic characterization, and gas sorption analyses allow us to sketch the following model of the structural evolution during progressing ALD.

Initially, the supraparticles exhibit a surface identity determined by the wet-chemical synthesis processes before and during spray-drying (**Figure 6**a). After initial nucleation (Figure 6b), ALD growth progresses with each cycle. Thereby, the surface functionality is changed as desired, leading to optimized material properties (Figure 6c). Upon further deposition, pore necks within the porous supraparticles become blocked, yielding an ongoing clogging of the structure, which restricts further deposition on internal surfaces within the supraparticles (Figure 6d). Due to the ALD clogging, an ALD overcoating on the external surface of the microparticle only is obtained upon further deposition (Figure 6e). It is thus essential to monitor the structural evolution during progressing ALD to obtain a functionalized but also accessible surface.

2.5. Magnetic Particle Spectroscopy as a Rapid Analysis Technique

By transferring this principle onto other types of supraparticles, the number of ALD cycles required to achieve optimum properties will depend on the size of nanoparticles used and the nanostructure synthesized, as both modify the porosity. Additionally, it depends on the ALD material chosen, as the thickness of deposited layers varies for different materials.[25] As shown here, the magnetic measurements utilized and/or gas sorption measurements are powerful tools to provide the required information and can be used for other material systems as well. Additionally, magnetic particle spectroscopy (MPS)[41] provides an ultrafast, on-the-fly method as a rapid option to gain similar information. In MPS, the magnetic properties are represented by a harmonic spectrum, which is obtained after fast Fourier transform of the voltage induced in a coil by magnetic powder or liquid samples submitted to an AC field. Due to the fast measurement speed of seconds and the sensitivity towards structural changes of supraparticles,[42] MPS has been very recently proven to be an emerging tool for deducing structural information about supraparticles indirectly due to their magnetic properties.[42–44] MPS was used to spectrally analyze the magnetization amplitude of supraparticles modified by ALD as a function of harmonics (**Figure 7**a).

Due to the measurement principle, the magnetization amplitude of higher harmonics is only affected by the nonlinear magnetization behavior of materials (such as ferri/ferromagnetic or the superparamagnetic materials used here) and not affected by diamagnetic or paramagnetic materials (such as aluminum oxide). Thus, upon normalization of the spectrum with respect to the fundamental frequency, the different signal declines (Figure 7a) indicate ALD-induced changes on the

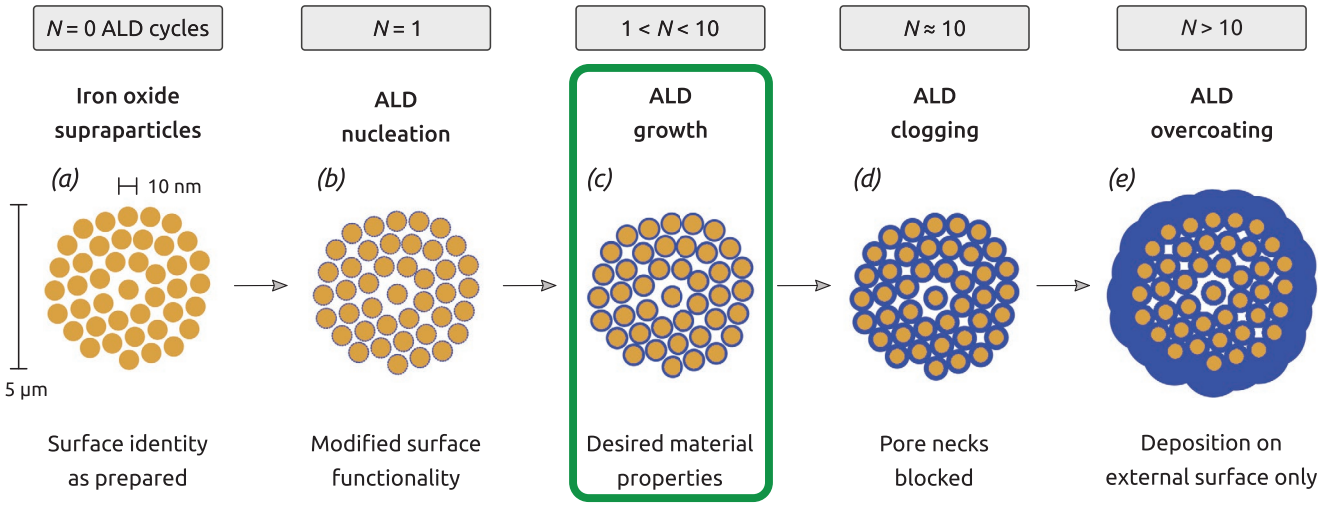

Figure 6. Schematic illustration of the structural evolution of iron oxide supraparticles with progressing ALD, based on all data presented here. a) Initially, iron oxide supraparticles exhibit a surface functionality determined by the wet-chemical synthesis processes before and during spray-drying. b,c) After initial ALD, the surfaces of all nanoparticles within the supraparticles are functionalized until they reach their desired material properties after more ALD growth. d) If further ALD cycles are performed, the deposition will fill and eventually block pore channels between individual nanoparticles. Clogged pores prevent gas precursor access and thereby hinder deposition. e) Subsequently, deposition occurs on the external microparticle surface only. While the state in (c) will be desired for optimal material functionality, the states (d) and (e) must be avoided to leave the deposited surface accessible and thus functional.

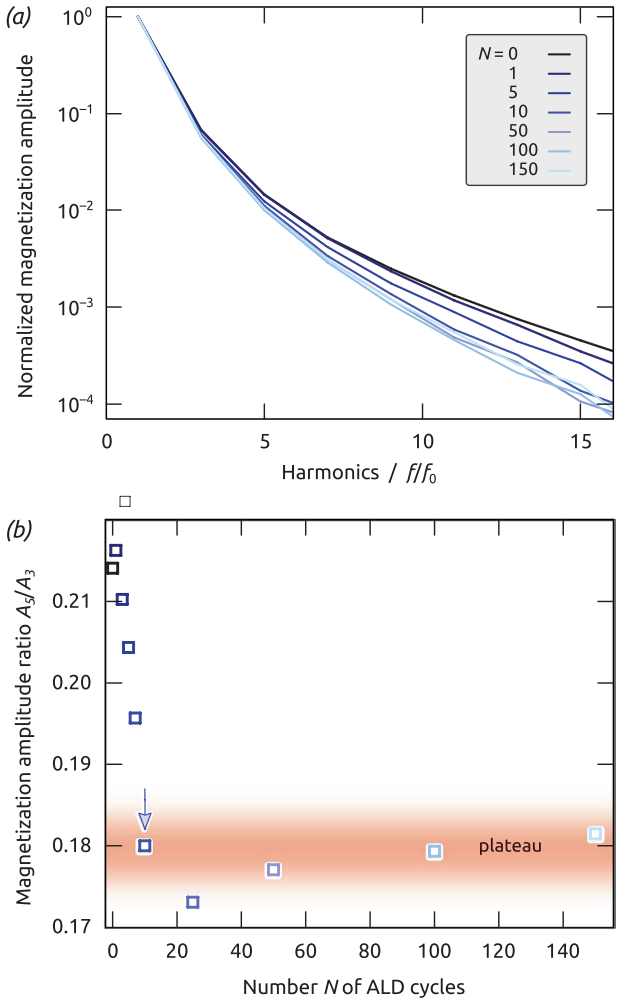

Figure 7. a) Normalized magnetization amplitude as a function of harmonics obtained from magnetic particle spectroscopy reveals a signal decay that becomes progressively faster with progressing ALD. b) Analyzing the magnetization amplitude ratio A_5/A_3 as a function of cycle number reveals an initially fast magnetization amplitude decay before a plateau is reached (the blue arrow indicates the onset of pore clogging with ten cycles of ALD). Thus, MPS is capable to sensitively obtain similar information as conventional magnetometer or gas sorption analyses in a few seconds only.

magnetic properties of the iron oxide supraparticles. With progressing ALD, the spectra decline faster, indicating that MPS is capable of resolving changes of the iron oxide supraparticles with progressing aluminum oxide deposition. As aluminum oxide does not significantly contribute to the magnetization amplitude intensity detected, the various spectra indirectly confirm its deposition on the internal supraparticle surfaces due to modified iron oxide nanoparticle surfaces. These in turn alter their magnetic properties, which might be explained by altered magnetic anisotropy, an increase in effective magnetic volume.[45,46] Due to the surface modification of the nanoparticles after their assembly, altered particle-particle distances can be prevented. Thus, this finding will be of interest for the countless researchers working on surface magnetism because it allows one to analyze the effect of surface modifications on the magnetic properties in detail and in the absence of undesired interferences by other effects. Upon analyzing the magnetization amplitude ratio of the fifth and the third harmonic (A_5/A_3) as a function of cycle number (Figure 7b), the trend described in other data sets is reproduced: a fast initial decay in magnetization amplitude followed by a plateau as soon as the clogged pores restrict deposition to the external surface of the supraparticles. Thus, MPS is also capable of identifying pore clogging of the supraparticles and provides an alternative characterization technique to determine the desired deposition with the great advantage of simple sample preparation and very fast measurement speed on the order of seconds.

2.6. Confirmation of Structural Evolution for Further ALD Materials

Toward a broader variety of material combinations, the flexibility in terms of material choices of ALD is demonstrated by the deposition of titanium dioxide (TiO_2) and zinc oxide (ZnO) as examples. The three oxides chosen here have been established and widely studied in the ALD field and hence give rise to a well-understood materials family. The deposition occurs typically in similar temperature windows (120–150 °C) and the same co-reactant (H_2O) is used for all three reactions. The precursors for Al_2O_3 and ZnO ALD, trimethylaluminum (TMA) and diethylzinc (DEZ), exhibit similar reactivities based on their comparable volatility and molecule size, whereas the precursor used for TiO_2 ALD, titanium(IV) tetraisopropoxide (TTIP), exhibits lower volatility based on its larger molecule size. Therefore, comparing the deposition of these three materials onto the supraparticles gives rise to a universal approach of combining spray-drying and ALD as complementary tools.

Magnetization curves (**Figure 8**a), zero-field-cooled/field-cooled measurements (Figure 8b), and MPS spectra (Figure 8c) were analyzed to characterize the geometric structural evolution upon deposition as a function of ALD cycles of these materials. It is well known that the atomic layer thickness deposited of the used materials varies due to their different GPC, which are affected by the size, volatility, and reactivity of the precursors molecules. To compensate for this, the magnetic characterization was performed as a function of ALD thickness determined by ellipsometry rather than by cycle number.

Most importantly, up to ≈2 nm ALD thickness, a fast change in saturation magnetization (a), blocking temperature (b) and magnetization amplitude ratio (c) was observed for all samples before they enter a plateau phase. Independently of the ALD material, pore clogging (Figure 8d) of the supraparticles occurred at similar thicknesses for different materials. The material deposition thus behaves similarly for all three materials. In addition to the variation of ALD material shown, the supraparticles utilized could be interchanged as well. As ALD is capable to modify all accessible surfaces within the deposition chamber, the size of the used supraparticles does not affect the ALD quality. However, different structures of the supraparticles such as larger pore channels will alter the amount of deposited material. As the general behavior (initial deposition on all surfaces with subsequent clogging) will still remain similar, the complementary tools presented will allow the experimentalist

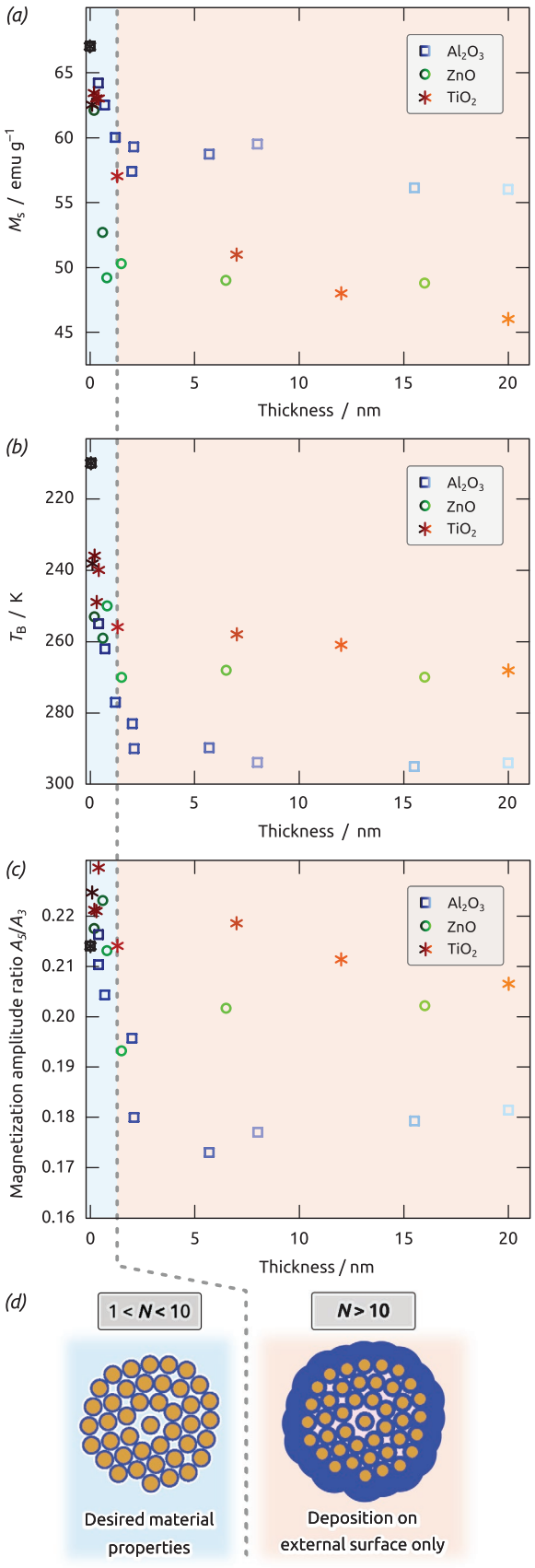

to deduce structural information for various supraparticle architectures. This opens up the powerful possibility to analyze the structural evolution of freely designed supraparticles by transferring this concept to a variety of material combinations due to the universality of ALD and spray-drying. The generality demonstrated here is of high significance to the design of advanced functional materials tailored for various applications.

3. Conclusion

In summary, supraparticles were assembled from iron oxide nanoparticles via spray-drying as a model substrate. It is shown that ALD is a versatile process to functionalize not only the external surface but also the internal surface within filigree porous supraparticles. The magnetic properties of iron oxide supraparticles are exploited to monitor the structural evolution upon progressing deposition of aluminum oxide with atomic resolution. The advantage of ALD to precisely control the masses deposited is essential in order to obtain optimum surface properties without complete pore clogging, which would make the functionality inaccessible otherwise. The structural evolution proposed is confirmed by detailed gas sorption analyses. In order to demonstrate the flexibility of ALD to confer supraparticles with a vast variety of surface functionalities, the successful deposition of titanium dioxide and zinc oxide is monitored and similar structural evolutions are observed. The powerful possibility to combine supraparticles consisting of freely chosen materials into a defined nanostructure as achievable by spray-drying, with desired surface functionalities determined by ALD will be transferred to other materials to address a wide variety of applications in future. To do so, it is demonstrated that magnetic particle spectroscopy has the potential to analyze the structural evolution within seconds.

4. Experimental Section

Synthesis of Iron Oxide Nanoparticles: Superparamagnetic iron oxide nanoparticles were obtained from a coprecipitation reaction. Iron(III) chloride hexahydrate ($FeCl_3 \cdot 6H_2O$, 10.80 g, 40 mmol, Sigma Aldrich, >99%) and iron(II) chloride tetrahydrate ($FeCl_3 \cdot 4H_2O$, 3.98 g, 20 mmol, Sigma Aldrich, >99%) were dissolved in deionized water (125 mL) and mixed with 5 wt% aqueous ammonia solution (NH_3(aq.), 125 g, Carl Roth 25% pure) in a static mixer (plastic spiral bell mixer 7700924, Nordson Deutschland GmbH) with the help of a peristaltic pump (Ismatech MCP, flow rate 1000 mL min^{-1}). The black precipitate was magnetically separated after 1 min and washed three times with deionized water to remove excess chemicals. Stabilization was

Figure 8. a) Saturation magnetization M_S obtained from magnetization curves, b) blocking temperature T_B obtained from zero-field-cooled/field-cooled, and c) magnetization amplitude ratios A_5/A_3 obtained from magnetic particle spectroscopy as a function of deposited thicknesses via ALD for aluminum oxide (Al_2O_3, squares), zinc oxide (ZnO, circles), and titanium dioxide (TiO_2, stars). All three characterization techniques complementarily indicate that the structural evolution within the supraparticles occurs similarly for all three materials. d) Reaching the plateau region after ≈2 nm layer thickness represents the deposition on external surfaces only due to pore clogging ($N > 10$). Desired material properties will be obtained when fewer ALD cycles ($1 < N < 10$) are performed.

performed by stirring the magnetic nanoparticles in an aqueous citric acid solution ($C_6H_8O_7 \cdot H_2O$, 0.05 M, 500 mL, Panreac AppliChem, ACS grade) for 5 min before magnetic separation and washing three times with ethanol. A stable ferrofluid with 1.5 wt% particles/total mass was obtained after redispersion in deionized water (500 mL).

Synthesis of Iron Oxide Supraparticles: Supraparticles were obtained by spray-drying the ferrofluid with a spray-dryer (B290 mini, Büchi Labortechnik AG). During spray-drying, droplets were finely atomized in a hot chamber, the solvent evaporates and spherical supraparticles were collected as a powder. Inlet temperature of the spray-dryer was set to 130 °C with a pump rate of 10%, a gas flow of 40 L min^{-1}.

ALD on Supraparticles: Silicon (100) wafers with 200 nm thermal oxide were purchased from Silicon Materials Inc. The metal precursors for ALD, TMA, DEZ, and TTIP were purchased from abcr GmbH, Merck KGaA, and Alfa Aesar, respectively, and used without further purification. Glass fiber filters (retention area ≥ 0.6 µm) were purchased from Carl Roth GmbH + Co. KG.

ALD of Al_2O_3, ZnO, and TiO_2 on Fe_3O_4 supraparticles was conducted on a GEMStar-6 XT ALD reactor from Arradiance. For the Al_2O_3, ZnO, and TiO_2 ALD, TMA, DEZ, and TTIP were used as metal precursors, respectively. Distilled purified H_2O was used as second precursor. For Al_2O_3 and ZnO gALD, both TMA and DEZ were kept at room temperature. For TiO_2 gALD, the TTIP was heated to 70 °C to achieve sufficient vapor pressure. In all three cases, the H_2O was kept at room temperature. The temperatures of metal precursor manifold, co-reagent manifold and reaction chamber were set to 100, 80, and 120 °C, respectively. The pulse, exposure, and purge durations for all three metal precursors and H_2O were 1, 60, and 120 s, respectively. During the deposition experiments, the Fe_3O_4 supraparticle powder was held inside a ceramic crucible and covered with a glass fiber filter using Kapton (polyimide) tape.

The thickness of the films deposited was derived from silicon wafers with a spectroscopic ellipsometer SENPro (SENTECH Instruments GmbH) in the wavelength range from 370 to 1050 nm under an angle of 70°. Data analysis was performed with the software SpectraRay 4.

Scanning Electron Microscopy: For SEM overview images, the supraparticle powder was prepared on a carbon pad and analyzed with a JSM-F100 (JEOL) with an acceleration voltage of 2 kV (field emission) and a secondary electron detector. For cross-section preparation, the supraparticle powder was embedded between two silicon wafers and cut with a cross-section polisher (JEOL). EDX analysis was performed as a line scan with 10 kV acceleration voltage.

Magnetic Characterization: Magnetization curves and ZFC/FC measurements were performed with a superconducting quantum interference device (SQUID) magnetometer MPMS 3 (Quantum Design Inc., San Diego, CA). Magnetization curves were obtained at 300 K in the range ±30 000 Oe (3 T). Measurement speed was set to 5 Oe s^{-1} in the range within ±5000 Oe and 50 Oe s^{-1} exteriorly.

For zero-field-cooled/field-cooled measurements, all samples were cooled to 30 K without external field after demagnetizing. After applying an external field of 10 Oe the measurement was conducted during temperature increase to 300 K and subsequent decrease to 30 K with 3 K min^{-1}.

MPS measurements were conducted on powder samples with a MPS unit (Pure Devices GmbH, Rimpar, Germany) in a sinusoidal alternating magnetic field of 20.1 kHz from ±300 Oe. The spectrum was generated by averaging five individual measurements with an acquisition time of 200 ms. A reference spectrum without sample was measured and automatically subtracted.

Gas Sorption Characterization: High-resolution nitrogen (77.4 K) isotherm measurements were performed using an Autosorb-iQ sorption instrument (Anton Paar Quantatec, Boynton Beach, FL). Before each sorption measurement samples were outgassed for 12 h under turbomolecular pump vacuum at 423 K.

Supporting Information

Supporting Information is available from the Wiley Online Library or from the author.

Acknowledgements

This work was financially supported by the BMBF NanoMatFutur Grant 03XP0149, which is gratefully acknowledged. S.M. acknowledges his doctoral scholarship funding of the German Federal Environmental Foundation (DBU). S.M. and K.M. thank BÜCHI Labortechnik AG for providing the spray-dryer equipment. Financial support was also provided by the European Research Council (ERC) in the ERC Consolidator Grant "Solacylin" (Grant Agreement No. 647281), and by FAU via the excellence cluster "Engineering of Advanced Materials" and the "Emerging Talents Initiative."

Open access funding enabled and organized by Projekt DEAL.

Conflict of Interest

The authors declare no conflict of interest.

Author Contributions

S.M. and V.K. contributed equally to this work. Magnetic characterization was performed by S.M., ALD experiments by V.K. and M.B., gas sorption experiments by C.C.C and M.T. Interpretation and conclusions were drawn by the respective authors and discussed with all authors. Coordination of the project was done by S.M., V.K., and M.B. and supervision of the overall project by J.B. and K.M. Initial publication draft was created by S.M., V.K., and M.B., refined with all authors and written by S.M., V.K., M.B., C.C.C., M.T., and K.M. Editing was performed by all authors. All authors proof-read the publication and have given approval to the final version of the manuscript.

Data Availability Statement

The data that support the findings of this study are available from the corresponding authors upon reasonable request.

Keywords

atomic layer deposition, spray-drying, supraparticles

Received: October 15, 2021
Revised: October 29, 2021
Published online: November 21, 2021

[1] R. Li, Y. Zhang, J. Tan, J. Wan, J. Guo, C. Wang, *ACS Appl. Mater. Interfaces* **2016**, *8*, 9384.
[2] F. Miller, S. Wintzheimer, J. Prieschl, V. Strauss, K. Mandel, *Adv. Opt. Mater.* **2021**, *9*, 2001972.
[3] M. Oppmann, M. Wozar, J. Reichstein, K. Mandel, *ChemNanoMat* **2019**, *5*, 230.
[4] M. Puddu, D. Paunescu, W. J. Stark, R. N. Grass, *ACS Nano* **2014**, *8*, 2677.
[5] S. Wintzheimer, T. Granath, M. Oppmann, T. Kister, T. Thai, T. Kraus, N. Vogel, K. Mandel, *ACS Nano* **2018**, *12*, 5093.
[6] S. Wintzheimer, J. Reichstein, P. Groppe, A. Wolf, B. Fett, H. Zhou, R. Pujales-Paradela, F. Miller, S. Müssig, S. Wenderoth, K. Mandel, *Adv. Funct. Mater.* **2021**, *31*, 2011089.
[7] J. Lacava, P. Born, T. Kraus, *Nano Lett.* **2012**, *12*, 3279.
[8] V. N. Manoharan, M. T. Elsesser, D. J. Pine, *Science* **2003**, *301*, 483.
[9] O. D. Velev, K. Furusawa, K. Nagayama, *Langmuir* **1996**, *12*, 2374.
[10] T. Brugarolas, F. Tu, D. Lee, *Soft Matter* **2013**, *9*, 9046.

[11] T. Kister, M. Mravlak, T. Schilling, T. Kraus, *Nanoscale* **2016**, *8*, 13377.
[12] W. Liu, M. Kappl, H.-J. Butt, *ACS Nano* **2019**, *13*, 13949.
[13] P. Biswas, D. Sen, S. Mazumder, C. B. Basak, P. Doshi, *Langmuir* **2016**, *32*, 2464.
[14] A. B. D. Nandiyanto, K. Okuyama, *Adv. Powder Technol.* **2011**, *22*, 1.
[15] K. Okuyama, M. Abdullah, I. W. Lenggoro, F. Iskandar, *Adv. Powder Technol.* **2006**, *17*, 587.
[16] H. Canziani, F. Bever, A. Sommereyns, M. Schmidt, N. Vogel, *ACS Appl. Mater. Interfaces* **2021**, *13*, 25334.
[17] S. Müssig, J. Reichstein, J. Prieschl, S. Wintzheimer, K. Mandel, *Small* **2021**, *17*, 2101588.
[18] L. Gradon, R. Balgis, T. Hirano, A. M. Rahmatika, T. Ogi, K. Okuyama, *J. Aerosol Sci.* **2020**, *149*, 105608.
[19] S. Zellmer, G. Garnweitner, T. Breinlinger, T. Kraft, C. Schilde, *ACS Nano* **2015**, *9*, 10749.
[20] A. B. D. Nandiyanto, T. Ogi, W.-N. Wang, L. Gradon, K. Okuyama, *Adv. Powder Technol.* **2019**, *30*, 2908.
[21] T. T. Nguyen, A. M. Rahmatika, M. Miyauchi, K. L. A. Cao, T. Ogi, *Langmuir* **2021**, *37*, 4256.
[22] K. Cao, J. Cai, B. Shan, R. Chen, *Sci. Bull.* **2020**, *65*, 678.
[23] S. M. George, *Chem. Rev.* **2010**, *110*, 111.
[24] R. W. Johnson, A. Hultqvist, S. F. Bent, *Mater. Today* **2014**, *17*, 236.
[25] R. L. Puurunen, *J. Appl. Phys.* **2005**, *97*, 121301.
[26] J. W. Elam, G. Xiong, C. Y. Han, H. H. Wang, J. P. Birrell, J. N. Hryn, M. J. Pellin, J. F. Poco, J. H. Satcher, *MRS Online Proc. Libr.* **2006**, *876*, 126.
[27] S. Haschke, Y. Zhuo, S. Schlicht, M. K. S. Barr, R. Kloth, M. E. Dufond, L. Santinacci, J. Bachmann, *Adv. Mater. Interfaces* **2019**, *6*, 1801432.
[28] S. K. Panda, H. Shin, *Atomic Layer Deposition of Nanostructured Materials*, Wiley-VCH, Weinheim, Germany, pp. 23–40.
[29] V. Cremers, R. L. Puurunen, J. Dendooven, *Appl. Phys. Rev.* **2019**, *6*, 021302.
[30] C. A. Wilson, R. K. Grubbs, S. M. George, *Chem. Mater.* **2005**, *17*, 5625.
[31] Y. Köseoğlu, *J. Magn. Magn. Mater.* **2006**, *300*, e327.
[32] W. Wu, Q. He, C. Jiang, *Nanoscale Res. Lett.* **2008**, *3*, 397.
[33] C. Stauch, S. Späth, T. Ballweg, R. Luxenhofer, K. Mandel, *J. Colloid Interface Sci.* **2017**, *505*, 605.
[34] M. Thommes, K. Kaneko, A. Neimark, J. Olivier, F. Rodriguez-Reinoso, J. Rouquerol, K. Sing, *Pure Appl. Chem.* **2015**, *87*.
[35] K. A. Cychosz, R. Guillet-Nicolas, J. García-Martínez, M. Thommes, *Chem. Soc. Rev.* **2017**, *46*, 389.
[36] C. Schlumberger, M. Thommes, *Adv. Mater. Interfaces* **2021**, *8*, 2002181.
[37] J. Landers, G. Y. Gor, A. V. Neimark, *Colloids Surf., A* **2013**, *437*, 3.
[38] M. Thommes, C. Schlumberger, *Annu. Rev. Chem. Biomol. Eng.* **2021**, *12*, 137.
[39] M. Thommes, B. Smarsly, M. Groenewolt, P. I. Ravikovitch, A. V. Neimark, *Langmuir* **2006**, *22*, 756.
[40] C. J. Rasmussen, A. Vishnyakov, M. Thommes, B. M. Smarsly, F. Kleitz, A. V. Neimark, *Langmuir* **2010**, *26*, 10147.
[41] S. Biederer, T. Knopp, T. F. Sattel, K. Lüdtke-Buzug, B. Gleich, J. Weizenecker, J. Borgert, T. M. Buzug, *J. Phys. D: Appl. Phys.* **2009**, *42*, 205007.
[42] S. Wintzheimer, S. Müssig, S. Wenderoth, J. Prieschl, T. Granath, F. Fidler, D. Haddad, K. Mandel, *ACS Appl. Nano Mater.* **2019**, *2*, 6757.
[43] S. Müssig, B. Kuttich, F. Fidler, D. Haddad, S. Wintzheimer, T. Kraus, K. Mandel, *Nanoscale Adv.* **2021**, *3*, 2822.
[44] S. Müssig, T. Granath, T. Schembri, F. Fidler, D. Haddad, K.-H. Hiller, S. Wintzheimer, K. Mandel, *ACS Appl. Nano Mater.* **2019**, *2*, 4698.
[45] T. J. Daou, J. M. Grenèche, G. Pourroy, S. Buathong, A. Derory, C. Ulhaq-Bouillet, B. Donnio, D. Guillon, S. Begin-Colin, *Chem. Mater.* **2008**, *20*, 5869.
[46] A. Ebbing, O. Hellwig, L. Agudo, G. Eggeler, O. Petracic, *Phys. Rev. B* **2011**, *84*, 012405.